

## Ballistic nano-devices for high frequency applications

S. Bollaert<sup>a,\*</sup>, A. Cappy<sup>a</sup>, Y. Roelens<sup>a</sup>, J.S. Galloo<sup>a</sup>, C. Gardes<sup>a</sup>, Z. Teukam<sup>a</sup>, X. Wallart<sup>a</sup>,  
J. Mateos<sup>b</sup>, T. Gonzalez<sup>b</sup>, B.G. Vasallo<sup>b</sup>, B. Hackens<sup>c</sup>, L. Berdnarz<sup>c</sup>, I. Huynen<sup>c</sup>

<sup>a</sup> IEMN-DHS, CNRS UMR 8520, Avenue Poincaré, BP 60069, 59652 Villeneuve d'Ascq, France

<sup>b</sup> Dpto Fisica Aplicad, Universidad de Salamanca, Salamanca, Spain

<sup>c</sup> Université Catholique de Louvain, Louvain-La-Neuve, Belgium

Available online 8 September 2006

### Abstract

In this paper, we present a study on three-terminal ballistic junction and their applications to rectifiers and MUX/DEMUX. Rectifying effect is observed up to 94 GHz at room temperature. Although THz frequency performance has been demonstrated by Monte Carlo simulation, the high impedance of the nano-device combined with the parasitic capacitances is a limiting factor.

© 2006 Published by Elsevier B.V.

**Keywords:** Ballistic; Indium phosphide; Nanostructures

### 1. Introduction

One of the possible approaches for overcoming the limits of traditional scaling when reaching the nanometer range (which has been the main engine of the progress of the semiconductor industry) is to use devices exploiting the ballistic transport of electrons. Ballistic devices fabricated using the GaAs/AlGaAs heterojunction operating at low temperature have been demonstrated [1,2]. However, recent works have achieved an important improvement using InGaAs channels with high indium content [3–8]: room temperature operation is possible since the mean free path of electrons is still larger than 100 nm, a possible size for actual lithography techniques. The high electron mobility of InGaAs (indium content higher than 50%), which is typically 15,000 cm<sup>2</sup>/Vs at room temperature and beyond 100,000 cm<sup>2</sup>/Vs at 77 K, is associated with momentum relaxation times of 0.3 ps and 2 ps respectively. Therefore, for nanometer length devices, the transit time can be made shorter than the momentum relaxation time. Moreover, InGaAs-based ballistic devices give the advantage of being compatible with advanced HEMT technology. Recent works report room temperature operation based on ballistic transport [3–8], in which electron phase coherence is not necessary, leading to less

sensitivity of process fluctuation. For example, three-terminal ballistic junctions, TBJ (T or Y shape) have been extensively studied as well as ballistic rectifiers. The non-linear behavior of these TBJs and especially the appearance of parabolic negative potential at the central branch, when biasing in push–pull fashion the left and right branches (in contrast with the zero central potential for diffusive structures) has been described in several papers and explained by Landauer–Büttiker formalism [9]. This parabolic response offers the possibility to realize ballistic rectifier, and can be useful in ballistic detector or ballistic frequency doubler. Due to the nanometer length associated with ballistic transport, intrinsic frequency operation of THz is expected. Rectifying effect in TBJ up to 20 GHz has been demonstrated at room temperature [10]. Digital circuit can also be developed using TBJ. Indeed the voltage of the central branch follows an “OR” logic as a function of the voltages applied on the two horizontal branches [11]. NAND has been also demonstrated at room temperature [12]. Recently, using this principle, a half adder was demonstrated [13]. Further advantage is the small area of the realized circuit.

Another new concept for the fabrication of a ballistic rectifying device has been introduced in [10], by inserting an obstacle (antidot) with triangular or diamond shape in the center of a ballistic cross junction. Intrinsic working frequency higher than 1 THz has been demonstrated by Monte Carlo simulations [8].

\* Corresponding author. Tel.: +33 03 20 19 78 58; fax: +33 03 20 19 78 92.  
E-mail address: [Sylvain.Bollaert@IEMN.Univ-Lille1.fr](mailto:Sylvain.Bollaert@IEMN.Univ-Lille1.fr) (S. Bollaert).

Moreover, rectifying effect has been reported by electrical measurements. In order to improve the functionality of TBJs, the introduction of a gate to control the electron flux in one branch has been described. Using gated TBJs, an inverter with low power and small area size can be designed. Recently, Monte Carlo simulation demonstrates the functionality of a single gated TBJs and the possibility of realizing 1 THz working frequency [14].

In this paper, we present results on TBJ and TBJ with additional Schottky gate. DC and microwave measurements are also given. In Section 2, fabrication process of ballistic devices is described. High resolution process is needed to achieve few hundred nanometer dimensions with dozen nanometers resolution. Thus, details will be given on ballistic device process. Then, in Section 3, electrical characterizations are presented and compared with Monte Carlo simulations, thus allowing us to relate the macroscopic results of the experiments with the microscopic behavior of electrons. Our model, based on a semi-classical transport description, is able to qualitatively reproduce the main features of the ballistic effects measured in basic devices like TBJ [7], thus demonstrating that coherent transport plays no role on the main characteristics of these devices. Results on gated TBJs are also presented. Finally, the microwave measurements are presented mainly on TBJs acting as RF to DC rectifiers. Their intrinsic functionality in THz frequency range is demonstrated by Monte Carlo simulation and the high frequency capability of a nanometer ballistic device is discussed.

## 2. Fabrication

### 2.1. Layer structure

Our devices are based on GaInAs/AlInAs heterostructure on InP substrate (Fig. 1). This heterostructure presents advantages of technological compatibility with HEMTs and good transport properties of the InGaAs channel at room temperature. The heterostructure was grown by Molecular Beam Epitaxy. The active layers consist of a 4000 Å InAlAs buffer layer, a 150 Å

Contact In <sub>0.53</sub> Ga <sub>0.47</sub> As 6 · 10 <sup>18</sup> /cm <sup>3</sup>	100Å
Barrier In <sub>0.52</sub> Al <sub>0.48</sub> As nid	150Å
Delta doping plane N <sub>delta</sub> Si	
Spacer In <sub>0.52</sub> Al <sub>0.48</sub> As nid	L <sub>s</sub> Å
Channel In <sub>0.7</sub> Ga <sub>0.3</sub> As	150 Å
Buffer InAlAs nid	4000Å
InP Si substrate	

Fig. 1. InP-based heterostructure used for fabrication of ballistic nano-devices.

Table 1

Hall measurements at room and nitrogen temperatures of the heterostructure used for ballistic nano-devices for different spacer thickness  $L_s$

$L_s$ (Å)	$N_\delta$ (10 <sup>12</sup> /cm <sup>2</sup> )	300 K		77 K	
		$\mu_H$ (cm <sup>2</sup> /Vs)	$N_H$ (10 <sup>12</sup> /cm <sup>2</sup> )	$\mu_H$ (cm <sup>2</sup> /Vs)	$N_H$ (10 <sup>12</sup> /cm <sup>2</sup> )
50	5	11,700	3.6	46,800	3
100	4.5	14,000	2.65	74,000	2.6
200	4	14,800	1.82	92,000	1.76

In<sub>0.7</sub>Ga<sub>0.3</sub>As channel, an undoped In<sub>0.52</sub>Al<sub>0.48</sub>As spacer, a silicon planar doping layer  $N_\delta$ , a 150 Å thick In<sub>0.52</sub>Al<sub>0.48</sub>As Schottky barrier layer and a 100 Å Silicon doped In<sub>0.53</sub>Ga<sub>0.47</sub>As cap layer ( $N_d = 6 \cdot 10^{12}/\text{cm}^2$ ). An indium content of 70% in the InGaAs channel is used in order to obtain high electron mobility and a mean free path still larger than 100 nm at room temperature [8], leading to ballistic or quasi-ballistic behavior for the device with the active dimensions around 100 nm. Several thicknesses  $L_s$  of spacer were tested in order to obtain a very high mobility without too much degrading the sheet density of the two-dimensional electron gas. In these structures, the delta-doped level  $N_\delta$  has been adjusted to avoid free diffusive electrons. Table 1 reports the Hall measurements data for different spacer thicknesses  $L_s$ . For high spacer thickness, the mobility increases particularly at low temperature. This mobility enhancement is directly related to a decrease of the Coulomb interaction and hence to an increase of the mean free path. This indicates that, for ballistic applications, the structure design can derive benefit from an increase of  $L_s$ . However the spacer thickness of 100 Å was chosen, because it offers the best compromise between the electron mobility and the sheet carrier density (Table 1).

### 2.2. Technological process

For the realization of passive ballistic devices, technological process is achieved as following: mesa etching to define the active region, ohmic contacts and finally bonding pads. To form ohmic contacts, Ni/Ge/Au/Ni/Au metals were evaporated and followed by rapid thermal annealing at 295 °C for 60 s. Typical ohmic contact resistance is 0.15 Ω mm. Bonding pads are defined by Ti/Au metallization. All the lithography has been performed by electron beam, except the bonding pads. The e-beam machine used is a LEICA EBPG5000+. The minimum resolution of this tool is 7 nm. The mask design and lithography process were optimized in order to reach best specifications in resolution and levels positioning. By appropriate method, we achieved an alignment precision of about 25 nm, which is comparable to the best specifications of our equipment (2–3 times the spot size).

The important point of this process is the mesa step, because it defines the active region of ballistic devices. To design the mesa, we used a high resolution negative resist called HSQ (HydrogenSilsesQuioxane). For the mesa etching, low-damage process is a key issue to avoid degradation of transport properties. We use two ways to define structure: one using wet

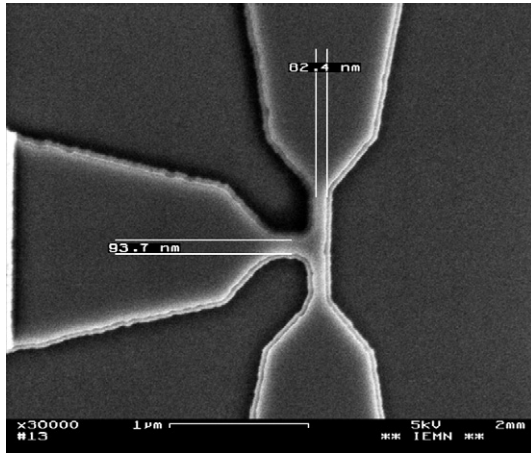


Fig. 2. SEM of realized TBJ using wet chemical etching for the definition of the active layer.

etching (highly diluted  $\text{H}_3\text{PO}_4/\text{H}_2\text{O}_2/\text{H}_2\text{O}$ ) and one using reactive ion etching (RIE,  $\text{CH}_4/\text{H}_2/\text{Ar}$ ). These gases have been chosen, because the etching rate of InGaAs and InAlAs materials is very low (a few 10 nm/min), which is fundamental for the control of the device dimensions. After the mesa etching, the HSQ resist is then removed by using buffered fluorhydric acid solution ( $\text{NH}_4\text{F}:\text{HF}$ ). Fig. 2 shows an SEM picture of a device realized by wet etching and Fig. 3 is a picture of a device realized by RIE. Several key parameters i.e. edge roughness, etching undercut and depletion width at the interface between air and semiconductor were studied, leading to etching choice and design rules (minimum achievable dimensions for our devices). The parameters comparison is summarized in Table 2. The interface air/semiconductor (possible degradation due to etching process) was determined using resistance measurement from many channels of different lengths and widths. We found a same  $W_d$  of about 40 nm for wet and dry etchings at room temperature. The last important point is the etching undercut determined by SEM observations. Undercut corresponds to lateral etching of materials under the resist mask. For RIE, measured dimensions are quite closed to the value of the mask,

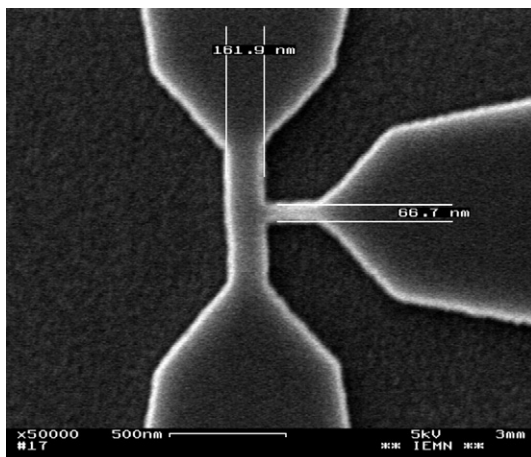


Fig. 3. SEM of realized TBJ using dry chemical etching for the definition of the active layer.

Table 2  
Parameters comparison between RIE and wet etching

$T=300\text{ K}$	RIE	Wet etching
Edges	Low roughness	High roughness layers under etching
Etching undercut	Measured dimensions closed to mask dimensions	>60 nm
Depletion width	$40\text{ nm} \pm 10\text{ nm}$	$40\text{ nm} \pm 10\text{ nm}$
Minimum conductive channel	$80\text{ nm} \pm 10\text{ nm}$	$200\text{ nm} \pm 10\text{ nm}$

but for wet etching, the undercut is about 60 nm (for an etching depth of about 80 nm). In Table 2, we report also the minimum active device width possible to achieve, defined as 2 times the sum of the depletion width  $W_d$  and the etching undercut. Minimum sizes are 80 nm and 200 nm for dry and wet etchings respectively. Moreover, edge roughness is lower using dry etching technique. Thus dry etching is preferred. Indeed it offers better dimension control, same induced damage and low roughness, essential for nanometer ballistic devices fabrication.

In order to control the electronic flow inside the TBJ, Schottky gate is added on top of one branch (Fig. 4). Those devices require an additional technological step for gate fabrication. Indeed Schottky level requires a selective recess. Thus mesa step has been modified. First selective recess etching, based on succinic acid (selectivity of InGaAs over InAlAs), is achieved. The entire wafer is recessed except ohmic contact zones. These zones are protected by a first level of HSQ. A second lithography step using HSQ is used to define the central part of the device. Then the RIE (previously presented) is achieved to complete the mesa. Finally both levels of HSQ resist are removed. For the gate, a conventional lithography process based on positive resist (PMMA) and Ti/Pt/Au gate metallization are used. The length of the gate has been fixed at 120 nm.

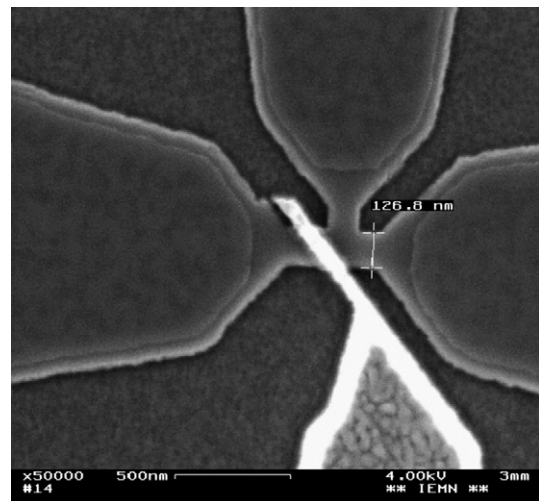


Fig. 4. SEM of realized TBJ with Schottky gate using wet chemical etching for the definition of the active layer.

### 3. Electrical results

#### 3.1. TBJ characterizations

TBJs have been measured in push–pull fashion (inset of Fig. 5). In this configuration, the right branch  $V_R$  is biased at DC voltage  $V_0$  and the left branch  $V_L$  at  $-V_0$ . The potential of the central branch  $V_C$  and the current flowing from the left to the right branch are measured and plotted in Fig. 5 versus the applied voltage  $V_0$ . This voltage  $V_C$  shows a bell shape versus the applied voltage  $V_0$ , lower than 250 mV and the evolution becomes linear for higher voltage  $V_0$ , corresponding to the saturation of the current. The bell shape is in agreement with previous published work [1–3], in which quantum model is used to demonstrate this evolution (Landauer–Büttiker). In order to understand the microscopic processes leading to the experimental measurements, 2D top-view Monte Carlo simulations of TBJ have been performed. Using similar geometry and adjusting some parameters (details of simulation in [8]), a good overall agreement with the intrinsic experimental results is found. The bell shape of  $V_C$  is related to space charge effects combined with ballistic transport of electron (Fig. 6). The space charge effect originates by the joint actions of the surface charge at the semiconductor–air interface, the background positive fixed charge (to account the ionized delta-doped in the different layers) and the inhomogeneous charge distribution associated with the ballistic motion of carriers injected at the contacts. Electron concentration and electric potential profiles along the middle of the horizontal branch of the TBJ for different bias push–pull conditions ( $V = V_L = -V_R$ ). The insets of panel (b) show the vertical potential profile in the middle of the central branch for several biasing, and the values of the potential at the bottom of this branch  $V_C$  and at the center of the junction  $V_{Hc}$  as a function of  $V$ .

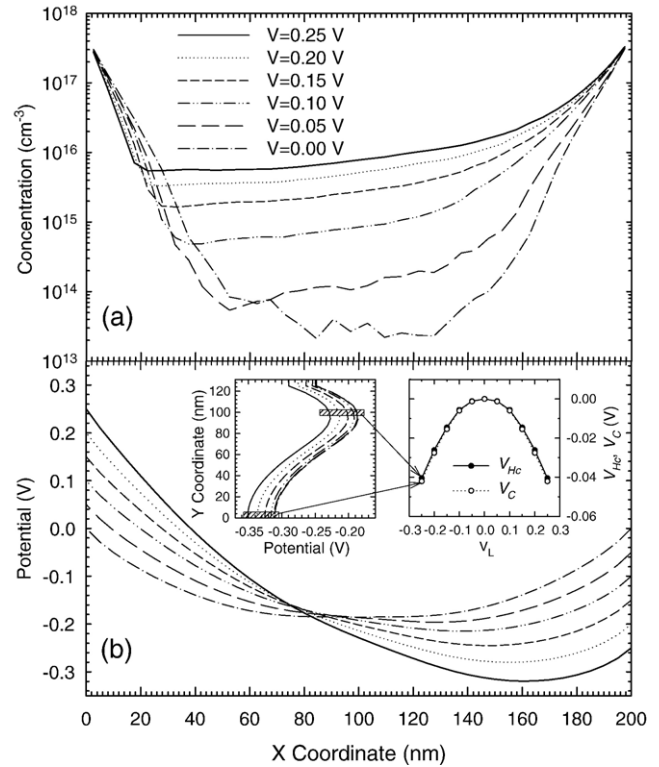


Fig. 6. (a) Electron concentration and (b) electric potential profiles along the middle of the horizontal branch of the TBJ for different bias push–pull conditions ( $V = V_L = -V_R$ ). The insets of panel (b) show the vertical potential profile in the middle of the central branch for several biasing, and the values of the potential at the bottom of this branch  $V_C$  and at the center of the junction  $V_{Hc}$  as a function of  $V$ .

versus geometry parameters, mainly width and length of the branches. Indeed in wide branch TBJ, the space charge effect disappears, leading to the suppression of the bell shape: potential in the central branch  $V_C$  remains zero. For long branch, diffusive transport occurs and gives also no negative bell shape.

Moreover this tool allowed explaining the linear evolution of the central potential  $V_C$ , as the applied voltage  $V_0$  exceeds a few hundred millivolts [7]. Indeed, at high  $V_0$ , intervalley transfers occur, leading to an increase of electron effective mass, and an accumulation domain appears near the anode. Thus as  $V_0$  increases, the additional potential drop is almost completely restricted to the accumulation region (near the anode), so the potential at the center of the horizontal branch (where  $V_C$  is measured) followed the variation of the cathode electrode (negative bias). This effect gives the linear shape of the  $V_C$  potential versus high applied bias  $V_0$  and the saturation of the  $I$ – $V$  curve (Fig. 5). We want to remark, even if the response of central potential is negative at low bias and high bias, frequency will be strongly limited for the latter. It means that high frequency performances related to ballistic transport are avoided at high bias voltage.

Quadratic dependence of central branch versus applied voltage of TBJ can be exploited in rectifier, mixer, frequency or doubler applications. Due to the ballistic character of transport combined with low dimension, high working intrinsic frequency is expected. In order to study microwave performance of TBJ, a

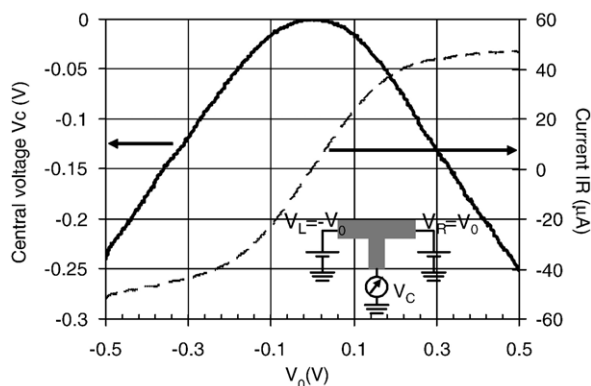


Fig. 5. Measured central potential  $V_C$  and current in horizontal branches as a function of the push–pull biasing ( $V_0 = V_L = -V_R$ ) in TBJ. Width of the branch is 120 nm, and length 200 nm. Inset represents a schematic of push–pull mode measurements.

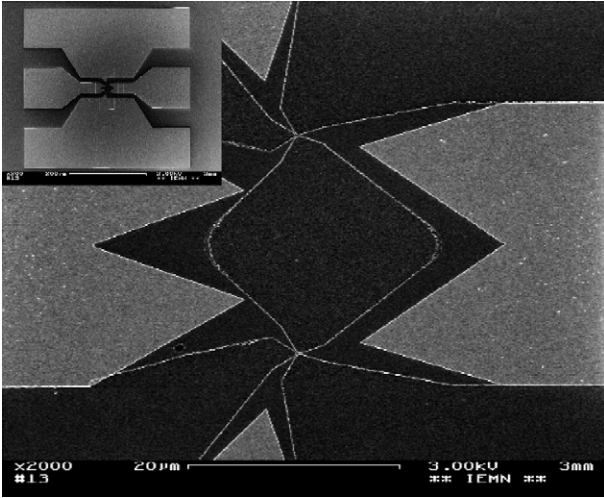


Fig. 7. Double TBJ with coplanar accesses for microwave measurements.

“double TBJ” was inserted in coplanar waveguide (Fig. 7). This structure allows standard two-port microwave measurements. Indeed we need only two coplanar accesses; one branch of each TBJ is connected to the ground of the coplanar waveguide. Different topologies of access waveguide have been studied. For the topology given in Fig. 7,  $S$ -parameters measurements have been achieved up to 50 GHz using an Agilent 8510 network analyser, at room temperature. Fig. 8 reports  $S$ -parameter  $S_{21}$  of the double TBJ of Fig. 7. Result indicates a strong dependence with frequency of the transmission coefficient. Moreover the level of transmitted signal is very low, indicating the poor matching between the 50Ω measurements environments used (network analyser, coplanar waveguide) compared with the high TBJ impedance (DC-resistance of 2.8 kΩ for 200 nm wide TBJs and 250 nm length). The evolution of the transmission parameter  $S_{21}$  versus frequency is mainly due to parasitic capacitance. The crosstalk capacitance is around 3 fF for this device. The parasitic capacitance transmits almost the HF signal between the left and the right branch causing a decrease of non-linear conversion. To expect to reach working frequency up to 40 GHz, parasitic crosstalk capacitance has to be lowering down 1.5 fF (Fig. 8), which can be obtained by optimization of the microwave

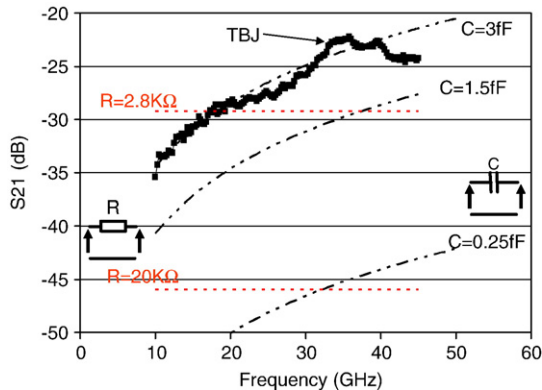


Fig. 8. Transmission scattering parameter  $S_{21}$  measured up to 50 GHz of a double TBJ. Calculated  $S_{21}$  of simple two-port devices constituted of crosstalk capacitance or resistance is also given.

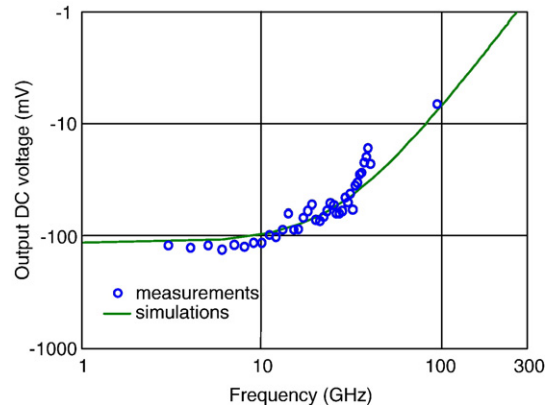


Fig. 9. DC voltage of output double TBJ acting as rectifier up to 94 GHz. The input power is  $-10$  dBm.

accesses to the TBJs. A second solution is the reduction of the TBJ impedance, by increasing the width of the TBJ or reducing the length. However the increase of the width will involve the reduction of non-linear effect, related to the lack of the bell shape [7].

Capability of DC rectifying has been also investigated on the double TBJ [15]. Input power is limited to 0.1 mW, to avoid electron transfer in the L-valley (no quadratic character). Two measurement setups were used: 3 GHz–40 GHz setup and 94 GHz setup. In the first setup a continuous wave source was used for HF signal generation and coaxial cables were used for connection of source and on-wafer probe. In the 94 GHz setup a Gunn diode source was used, together with waveguide connections between source and coplanar probe. Coplanar accesses have been optimized to reduce crosstalk capacitance. Fig. 9 reported DC-voltage at the output of the double TBJ versus frequency, indicating that rectifying effect is possible for frequency above 100 GHz, even if efficiency is degraded by parasitic capacitance. This measurement is compared to a non-linear model developed on Agilent ADS [15]. A good agreement is observed. The model shows that the frequency dependence observed in conversion experiments is due mainly to extrinsic crosstalk capacitances and access resistances.

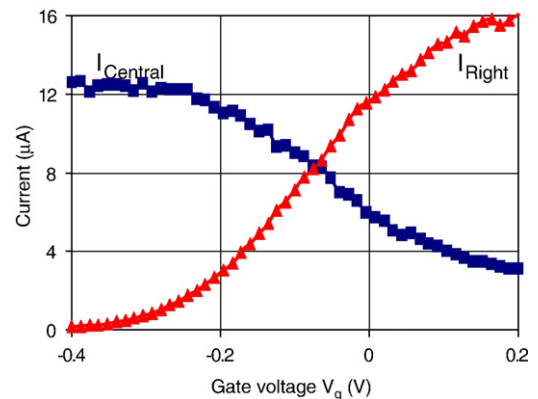


Fig. 10. Current of the central ( $I_{\text{central}}$ , square) and the right ( $I_{\text{right}}$ , triangle) branches versus applied gate voltage  $V_g$  of a TBJ with Schottky.

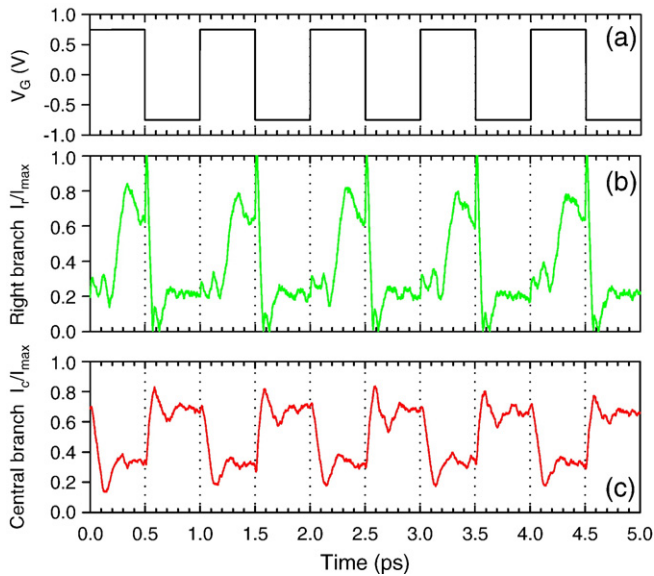


Fig. 11. Current of the central ( $I_{\text{central}}$ ) and the right ( $I_{\text{right}}$ ) branches versus square wave applied gate voltage  $V_g$  of a TBJ with Schottky. The frequency is 1 THz.

### 3.2. TBJ with gate

Motivation of this device is to realize a ballistic MUX/DEMUX for high bit rate communication [14]. The device is constructed by placing a Schottky gate on the top of one of the branches as shown in Fig. 4. The gate electrode is used to control the electron flux from one branch to another. Schottky gate allows us to use a lower bias to control the current, as previous work using side gate [5]. Fig. 10 gives the DC-characteristics of a gated TBJ. The right and central branches are biased to 200 mV, and the left branch is fixed at ground. When a low voltage is applied to the gate ( $-0.4$  V), the current in the right electrode is switched off (Fig. 10). As a consequence the left branch current flows toward the central branch. On the contrary when the gate potential is increased, most of the current is going from the left branch to the right branch. The gated TBJ acts as a routing device. Due to the ballistic behavior of this device, high intrinsic frequency of operation can be expected for this device. Monte Carlo simulation [14] predicted working switching frequency up to THz. This is illustrated (Fig. 11) by current in central and right branches plotted versus an input square wave signal at 1 THz applied to the gate electrode. We can observe on this graph the ability of the structure to perform THz MUX/DEMUX function. This result has to be confirmed with high frequency measurements, using proper high frequency accesses.

## 4. Conclusion

To summarize, ballistic devices based on three-terminal ballistic junctions have been studied and fabricated using high

resolution nanolithography. Using TBJ, quadratic response in push–pull mode operation has been demonstrated at room temperature. This behavior is to the combination of space charge effect and ballistic character of the electrons. Latter offers the possibility of mixing or rectifying applications up to THz frequency. Although DC-rectifying effect has been observed up to 94 GHz, extrinsic parasitic capacitance associated with the high intrinsic impedance of this nano-device drastically limits the performance. Finally adding a Schottky gate to TBJ permits the realization of ballistic MUX/DEMUX, and Monte Carlo simulation indicates the capability of THz working frequency. However this high frequency behavior will require careful design of microwave access, as mentioned for TBJ.

## Acknowledgements

This work has been partially supported by the European Commission through the NANOTERA project IST-2001-32517 and French Research Ministry through project ACI. This work is also supported by IRCICA, Dirección General de Investigación (Ministerio de Educación y Ciencia), FEDER (project TEC2004-05231) and Consejería de Educación de la JCyL (project SA044A05).

## References

- [1] L. Worschech, H.Q. Xu, A. Forchel, L. Samuelson, Appl. Phys. Lett. 79 (2001) 3287.
- [2] A.M. Song, A. Lorke, A. Kriele, J.P. Kothaus, W. Wegscheider, M. Bichler, Phys. Rev. Lett. 80 (1998) 3831.
- [3] K. Hieke, M. Ulfward, Phys. Rev., B 62 (2000) 16727.
- [4] A.M. Song, P. Omling, L. Samuelson, W. Seifert, I. Shorubalko, H. Zirath, Jpn. J. Appl. Phys. 40 (2001) L909.
- [5] I. Shorubalko, H.Q. Xu, I. Maximov, D. Nilsson, P. Omling, L. Samuelson, W. Seifert, IEEE Electron Device Lett. 23 (2002) 377.
- [6] I. Shorubalko, H.Q. Xu, I. Maximov, P. Omling, L. Samuelson, W. Seifert, Appl. Phys. Lett. 79 (2001) 1384.
- [7] J. Mateos, B.G. Vasallo, D. Pardo, T. González, E. Pichonat, J.S. Galloo, S. Bollaert, Y. Roelens, A. Cappy, IEEE Electron Device Lett. 25 (2004) 235.
- [8] J. Mateos, B.G. Vasallo, D. Pardo, T. González, J.S. Galloo, S. Bollaert, Y. Roelens, A. Cappy, IEEE Trans. Electron Devices 50 (2003) 1897.
- [9] T. Palm, J. Appl. Phys. 74 (5) (1993 (Sept.)) 3551.
- [10] L. Worschech, F. Fischer, A. Forchel, M. Kamp, H. Schweizer, Jpn. J. Appl. Phys. 40 (2001) L867.
- [11] T. Palm, L. Thülen, Jpn. J. Appl. Phys. 79 (10) (1996 (May)) 8076.
- [12] H.Q. Xu, et al., IEEE Electron Device Lett. 25 (4) (2004 (April)) 164.
- [13] L. Worschech, et al., Appl. Phys. Lett. 83 (12) (2003 (Sept.)) 2462.
- [14] J. Mateos, B.G. Vasallo, D. Pardo, T. González, J.S. Galloo, S. Bollaert, A. Cappy, Nanotechnology 14 (2003) 117.
- [15] Lukasz Bednars, Rashmi, Benoît Hackens, Ghania Farhi, Vincent Bayot, Isabelle Huynen, Jean-Sébastien Galloo, Yannick Roelens, Sylvain Bollaert, Alain Cappy, Microelectron. Eng. 81 (2005) 194.